Applied Mathematical Modelling 34 (2010) 2493–2507

Contents lists available at ScienceDirect

Applied Mathematical Modelling

journal homepage: www.elsevier.com/locate/apm

Nonlinear dynamic analysis of a hybrid squeeze-film damper-mounted rigid rotor lubricated with couple stress fluid and active control

Cai-Wan Chang-Jian [a,*], Her-Terng Yau [b], Jiann-Lin Chen [a]

[a] Department of Mechanical and Automation Engineering, I-Shou University, 1, Section 1, Hsueh-Cheng Road, Ta-Hsu Hsiang, Kaohsiung County 840, Taiwan, ROC
[b] Department of Electrical Engineering, Far-East College, No. 49, Jung-Hwa Road, Hsin-Shih Town, Tainan County 744, Taiwan, ROC

ARTICLE INFO

Article history:
Received 28 January 2008
Received in revised form 12 November 2009
Accepted 13 November 2009
Available online 24 December 2009

Keywords:
Hybrid squeeze-film damper
Couple stress fluid
Active control

ABSTRACT

The hybrid squeeze-film damper bearing with active control is proposed in this paper and the lubricating with couple stress fluid is also taken into consideration. The pressure distribution and the dynamics of a rigid rotor supported by such bearing are studied. A PD (proportional-plus-derivative) controller is used to stabilize the rotor-bearing system. Numerical results show that, due to the nonlinear factors of oil film force, the trajectory of the rotor demonstrates a complex dynamics with rotational speed ratio s. Poincaré maps, bifurcation diagrams, and power spectra are used to analyze the behavior of the rotor trajectory in the horizontal and vertical directions under different operating conditions. The maximum Lyapunov exponent and fractal dimension concepts are used to determine if the system is in a state of chaotic motion. Numerical results show that the maximum Lyapunov exponent of this system is positive and the dimension of the rotor trajectory is fractal at the non-dimensional speed ratio $s = 3.0$, which indicate that the rotor trajectory is chaotic under such operation condition. In order to avoid the nonsynchronous chaotic vibrations, an increased proportional gain is applied to control this system. It is shown that the rotor trajectory will leave chaotic motion to periodic motion in the steady state under control action. Besides, the rotor dynamic responses of the system will be more stable by using couple stress fluid.

1. Introduction

The fluid film bearing is a mechanical component, which has a strong nonlinearity. This is particularly true of squeeze-film damper bearings. Squeeze-film damper bearings are actually a special type of journal bearing with its journal mechanically prevented from rotating but free to vibrate within the clearance space. The squeezing action produces hydrodynamic forces in the fluid film. A squeeze-film damper bearing can be designed such that the journal can statically find its own position with in the clearance or be held centrally within the clearance by retaining springs. If the retaining springs are not used, the influence of contact and wear at zero speed will occur and it will add to the complexity of analysis of squeeze-film damper bearing. In a squeeze-film damper bearing-rotor system, the fluid support pressure is generated entirely by the motion of the journal and depends on the viscosity of the lubricating fluid. However, the hydrodynamic pressure around the bearing is nonlinear. It may cause fairly large vibrations of the rotor complicating the analysis of this system.

Chen and Yau [1] made a quite comprehensive simulation and found the chaotic behavior in a flexible rotor supported by oil film bearings with non-linear suspension. It also shows that due to non-linear factors, though the dynamic equation of the

* Corresponding author. Tel.: +886 7 6577711x3231.
E-mail address: cwchangjian@mail.isu.edu.tw (C.-W. Chang-Jian).

0307-904X/$ - see front matter © 2009 Elsevier Inc. All rights reserved.
doi:10.1016/j.apm.2009.11.014

Nomenclature

B	bearing parameter $= \frac{6\mu R^2 L^2}{m\delta^3\omega_n}$
d	viscous damping of the rotor disk
D	$\frac{d}{m\omega_n}$
e	damper eccentricity = $\varepsilon\delta$
f_x, f_y	components of the fluid film force in horizontal and vertical coordinates
F_r, F_t	components of the fluid film force in radial and tangential directions
h	oil film thickness, $h = \delta(1 + \varepsilon\cos\theta)$
k	stiffness of the retaining springs
k_d	proportional gain of PD controller
k_p	derivative gain of PD controller
L	bearing length
m	masses lumped at the rotor mid-point
O_m	center of rotor gravity
O_b, O_j	geometric center of the bearing and journal
$p(\theta)$	pressure distribution in the fluid film
p_s	pressure of supplying oil
$p_{c,i}$	pressure in the static pressure chamber
$Q_{in,i}$	the volumetric flow rate into oil chamber i (i = 1–4) from the controllable orifice
R	inner radius of the bearing housing
r	radius of the journal
r, t	radial and tangent coordinates
s	speed parameter $= \frac{\omega}{\omega_n}; \omega_n = \sqrt{\frac{k}{m}}$
U	$\frac{\rho}{\delta}$
x, y, z	horizontal, vertical and axial coordinates
x_0, y_0	damper static displacements
X, Y, X_0, Y_0	x/δ, y/δ, x_0/δ, y_0/δ
ρ	mass eccentricity of the rotor
ϕ	rotational angle ($\phi = \omega t$)
ω	rotational speed of the shaft
φ_b	angle displacement of line O_bO_j from the x-coordinate (see Fig. 1)
Ω	$\dot{\varphi}_b$
δ	radial clearance = $R - r$
θ	the angular position along the oil film from line O_1O_3 (see Fig. 1)
μ	oil dynamic viscosity
ε_0	$\sqrt{X_0^2 + Y_0^2}$
β	distribution angle of static pressure region
$(\bullet)$, $(')$	derivatives with respect to t and ϕ

bearing center and the rotor center are coupled, the trajectory of the rotor center demonstrates steady-state symmetric motion even when the trajectory of the bearing center is in a state of disorder. Nikolajsent and Holmes [2] reported their observation of nonsynchronous vibrations in a test rig of a flexible, symmetric rotor on two identical plain journal bearings supported by centralized squeeze-film dampers. Zhao et al. [3] discussed the subharmonic and quasi-periodic motions of an eccentric squeeze-film damper-mounted rigid rotor system. Chang-Jian and Chen [4–8] presented a series of papers discussing about flexible rotor supported by journal bearings under nonlinear suspension and also combined with rub-impact effect, turbulent effect and micropolar lubricant into consideration. They found very bountiful non-periodic responses occurring in rotor-bearing systems and the studies would help engineers or scientists escape undesired motions in either designing or operating rotor-bearing systems.

Many kinds of lubricants are non-Newtonian fluids in the scientific and engineering application. It can make the viscosity of the lubricant to be independent of the temperature. With the development of modern machine elements the increasing use of complex fluids as lubricants has been emphasized. There were also many significant studies the performance of non-Newtonian fluids. Oliver [9] had found that the presence of dissolved polymer in the lubricant could increase the load carrying capacity and decrease the friction. Spikes [10] showed that the base oil blending with additives could reduce the friction and the surface damage in elastohydrodynamic contacts. Because of the behavior of the complex fluids violates the linear shear stress-rate relationship, it fails to describe the rheological behavior of the non-Newtonian fluid. Therefore a different micro-continuum theory has been developed to better describe the rheological behavior of the non-Newtonian fluid. Stokes [11] proposed a simplest theory called the Stokes micro-continuum theory and which could be used for the

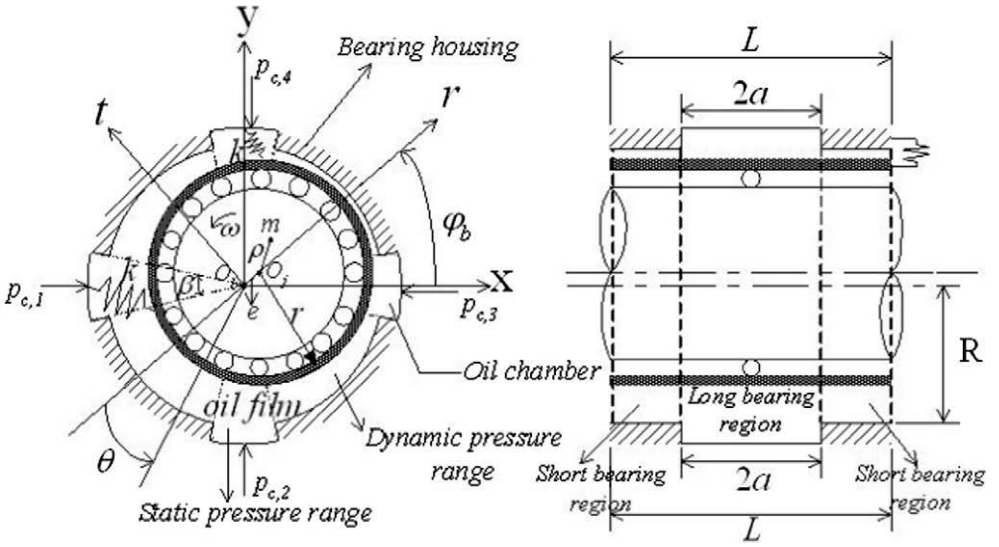

Fig. 1. Cross section of a rigid rotor supported by a hybrid squeeze film damper.

couple stress fluid. This kind of couple stress model is intended to take account of the particle-size effects, and it is also very useful in the applications of science and engineering. Thus there are more and more researches focusing on it and analyzing its performance. Ramanaiah [12] applied the couple-stress fluid model to analyze the long slider bearing. Gupta and Sharma [13] also used the couple-stress fluid model to carry out on hydrostatic thrust bearings. Shehawey and Mekheimer [14] applied the couple stress model to analyze the peristalsis problem for its relative mathematical simplicity. Das [15] proposed the analysis of elastohydrodynamic theory of line contacts. Das [16] studied the slider bearing lubricated with couple stress fluids in magnetic field and observed that both the values of the maximum load capacity and the corresponding inlet-outlet film ratio depend on couple stress, magnetic parameters and the shape of bearings. Lin [17] investigated the squeeze film characteristics of long partial journal bearings lubricated with couple stress fluid using the Stokes microcontinuum theory. Meanwhile Lin [18] also studied the static and dynamic behaviour of pure squeeze films in short journal bearings lubricated with the couple stress fluid, and the results showed that the effect of the couple stress could improve the dynamic stiffness and damping characteristics, and reduce the pumping power due to the decrease of the flow rate. Lin [19,20] performed investigations on externally pressurized circular step thrust bearings and linear stability analysis of rotor-bearing system lubricated with couple stress fluids. According to his research results, it was found that the rotor-bearing system with the couple stress fluid is more stable than the usage of the conventional Newtonian lubricant. Naduvinamani et al. [21] also presented the theoretical investigations of the rheological effects of the couple stress fluids on the static and dynamic behaviors of the pure squeeze films in the porous journal bearings.

The present paper analyzes a hybrid squeeze-film damper-mounted rigid rotor lubricated with couple stress fluid. The nonlinear dynamic equations are solved using the fourth order Runge-Kutta method. The dynamic trajectories, power spectrum, Poincaré maps, bifurcation diagrams, fractal dimension and the maximum Lyapunov exponent are applied to analyze the dynamic of the whole system.

2. Mathematical modeling

Fig. 1 shows a rigid rotor supported on a hybrid squeeze-film damper (HSFD) in parallel with retaining springs. The bearing consists of four hydrostatic chambers and four hydrodynamic regions. The oil film supporting force is dependent on the integrated action of hydrodynamic pressure and hydrostatic pressure of HSFD. The structure of this kind bearing should be popularized to consist of $2N$ ($N = 2, 3, 4, \ldots$) hydrostatic chambers and $2N$ hydrodynamic regions. In this study, oil pressure distribution model in the HSFD is proposed to integrate the pressure distribution of dynamic pressure region and static pressure region as described in Section 2.2.

2.1. Rotor dynamics equation

The equations of rotor motion in the Cartesian coordinates can be written as

$$m\ddot{x} + d\dot{x} + kx = m\rho\omega^2 \cos\omega t + f_x + kx_0, \tag{1}$$

$$m\ddot{y} + d\dot{y} + ky = m\rho\omega^2 \sin\omega t + f_y + ky_0. \tag{2}$$

The origin of the o-*xyz*-coordinate system is taken to be the bearing center O_b. Dividing these two equations by $mc\omega^2$ and defining a non-dimensional time $\phi = \omega t$ and a speed parameter $s = \frac{\omega}{\omega_n}$, one obtains the following non-dimensionalized equations of motion:

$$X'' + \frac{D}{s}X' + \frac{1}{s^2}X = U\cos\phi + \frac{B}{s}\left(\frac{XF_r - YF_\tau}{\varepsilon}\right) + \frac{X_0}{s^2}, \tag{3}$$

$$Y'' + \frac{D}{s}Y' + \frac{1}{s^2}Y = U\sin\phi + \frac{B}{s}\left(\frac{YF_r + XF_\tau}{\varepsilon}\right) + \frac{Y_0}{s^2}. \tag{4}$$

2.2. Solution of instant pressure distribution

The non-Newtonian Reynolds-type equation can be performed as follows [12]

$$\frac{\partial}{\partial x}\left(g(h,l)\frac{\partial p}{\partial x}\right) + \frac{\partial}{\partial z}\left(g(h,l)\frac{\partial p}{\partial z}\right) = 6\mu U\frac{\partial h}{\partial x} + 12\mu\frac{\partial h}{\partial t}, \tag{5}$$

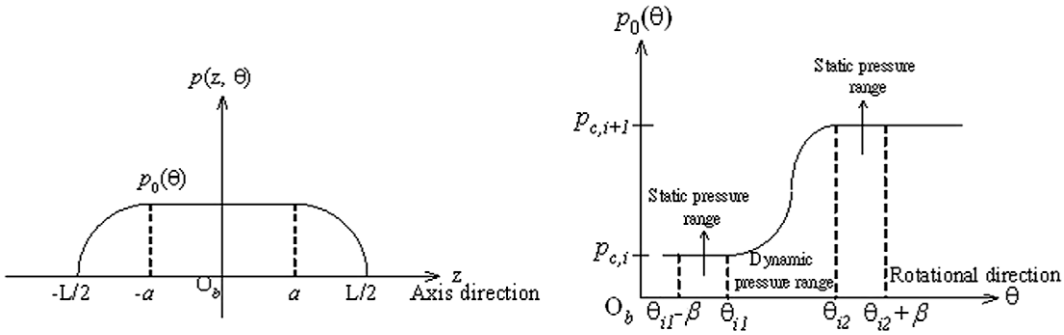

Fig. 2. The pressure distribution of HSFD in axis direction and rotational direction ($-a \leqslant z \leqslant a$) respectively.

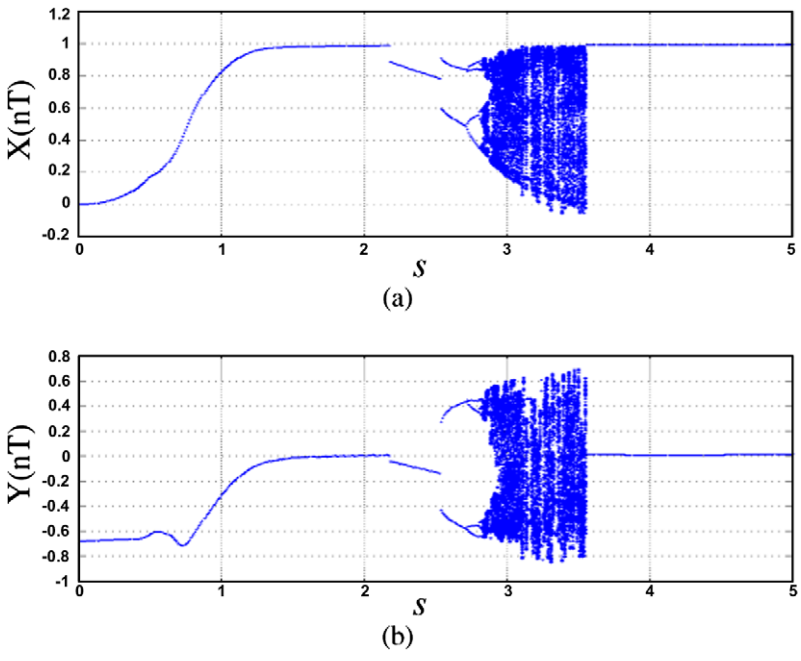

Fig. 3. Bifurcation diagram of $X(nT)$ (a) and $Y(nT)$ (b) versus rotor speed s ($l^* = 0.0$).

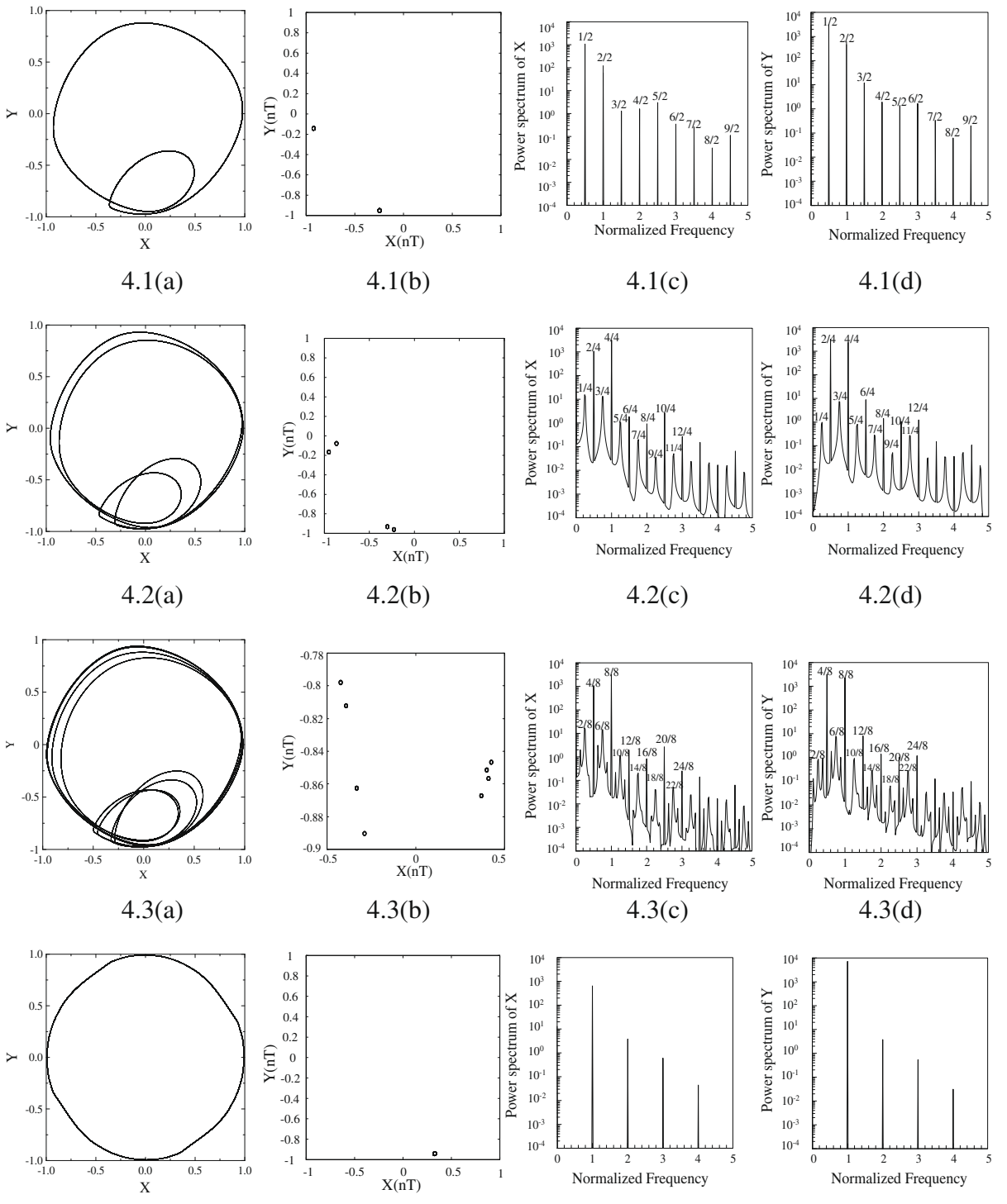

Fig. 4. The trajectory of rotor at $s = 2.7, 2.8, 2.82, 4.0$ (4.1(a)–4.4(a)); Poincaré section projected onto the $X(nT)$–$Y(nT)$ plane (4.1(b)–4.4(b)); displacement power in X and Y directions (4.1(c)–4.4(c) and 4.1(d)–4.4(d)).

where $g(h,l) = h^3 - 12l^2h + 24l^3\tanh\left(\frac{h}{2l}\right), \frac{\partial h}{\partial x} = -\frac{c\varepsilon}{R}\sin\theta, \frac{\partial h}{\partial t} = c\dot{\varepsilon}\cos\theta + c\varepsilon\dot{\varphi}\sin\theta, x = R\theta, U = R\omega, \varepsilon = \frac{e}{c}$ and $h = c(1 + \varepsilon\cos(\gamma - \varphi(t))) = c(1 + \varepsilon\cos\theta)$. Thus, $g(h,l)$ can also be expressed as $g(h,l) = c^3(1+\varepsilon\cos\theta)^3 - 12l^2c(1+\varepsilon\cos\theta) + 24l^3\tanh\left(\frac{c(1+\varepsilon\cos\theta)}{2l}\right)$,

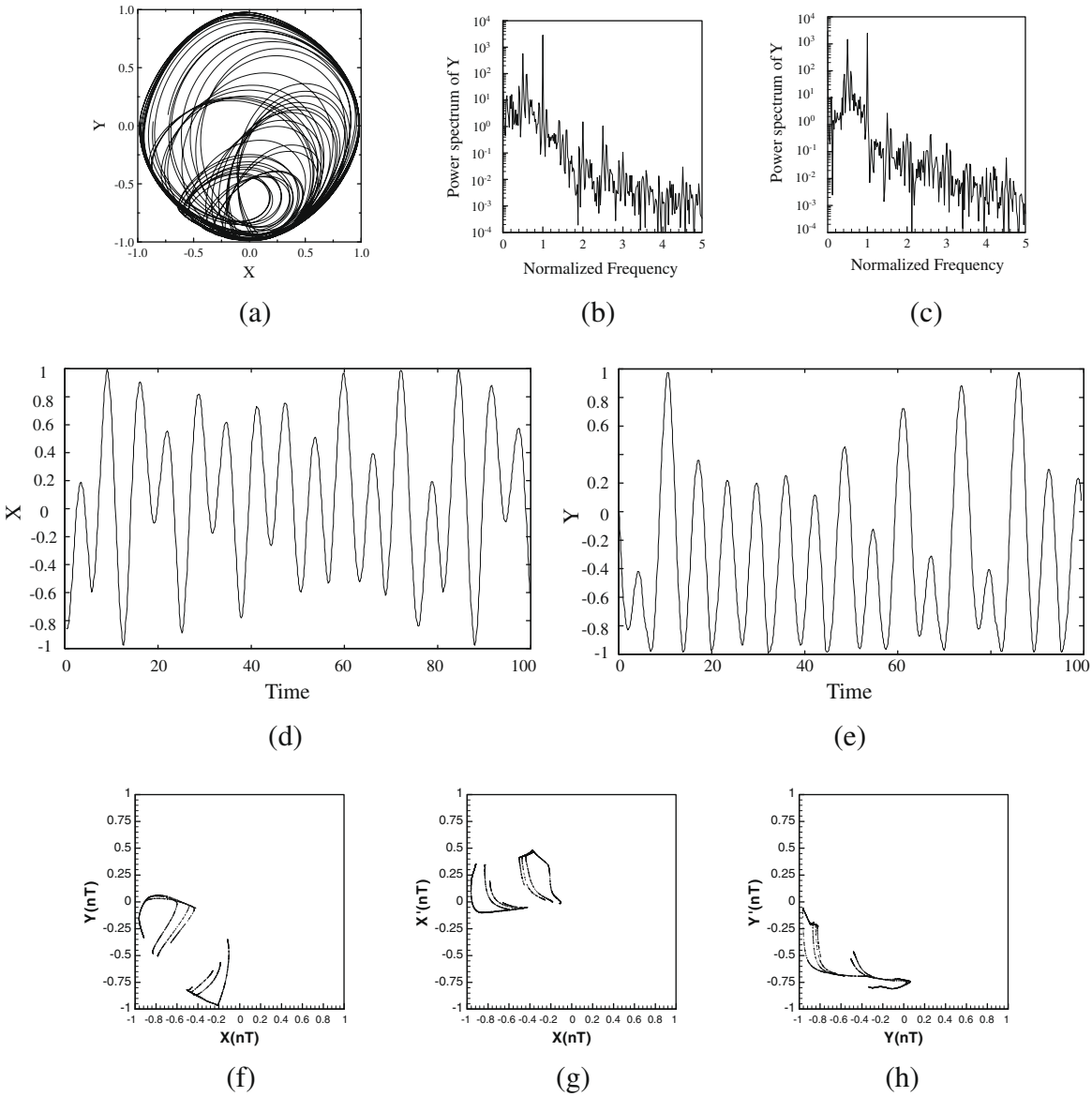

Fig. 5. Aperiodic motion of bearing center at $s = 3.0$; (a) rotor trajectory; (b) and (c) displacements power spectrum; (d) and (e) time series of rotor trajectory; (f)–(h) Poincare' maps.

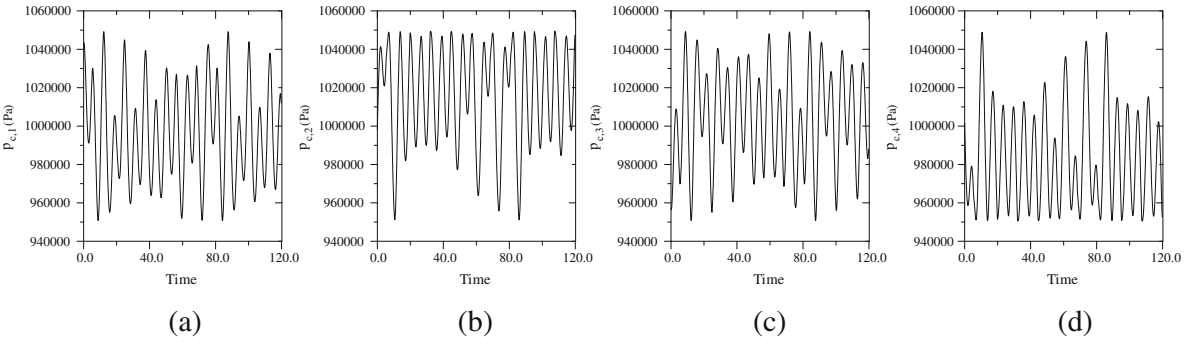

Fig. 6. Pressure distribution in the static pressure chamber at $s = 3.0$.

where $l = \left(\frac{\eta}{\mu}\right)^{1/2}$, in which μ is the classical viscosity parameter and η is a new material constant peculiar to fluids with couple stresses. The Reynolds equation can then be rewritten as

$$\frac{\partial}{R\partial\theta}\left(g(h,l)\frac{\partial p}{R\partial\theta}\right)+\frac{\partial}{\partial z}\left(g(h,l)\frac{\partial p}{\partial z}\right)=-6\mu\omega c\varepsilon\sin\theta+12\mu(c\dot{\varepsilon}\cos\theta+c\varepsilon\dot{\varphi}\sin\theta). \tag{6}$$

Applying the short-bearing approximation (i.e.$\frac{L}{D}<0.25$ and $\frac{\partial p}{\partial\theta}\ll\frac{\partial p}{\partial z}$), $\frac{\partial p}{\partial\theta}$ can be neglected with respect to $\frac{\partial p}{\partial z}$ so as to simplify the Reynolds differential equation. The following equation can then be introduced:

$$\frac{\partial^2 p}{\partial z^2}=\frac{-6\mu\omega c\varepsilon\sin\theta+12\mu(c\dot{\varepsilon}\cos\theta+c\varepsilon\dot{\varphi}\sin\theta)}{g(h,l)}, \tag{7}$$

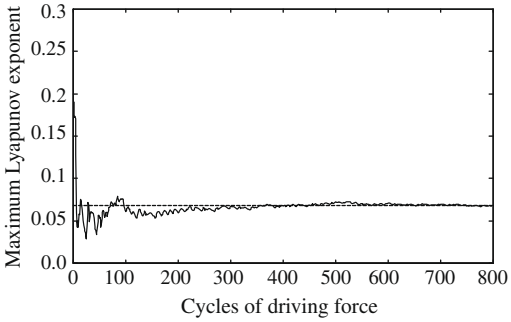

Fig. 7. The maximum Lyapunov exponent plotted as a function of the number of drive cycles at $\boldsymbol{s}$ = 3.0.

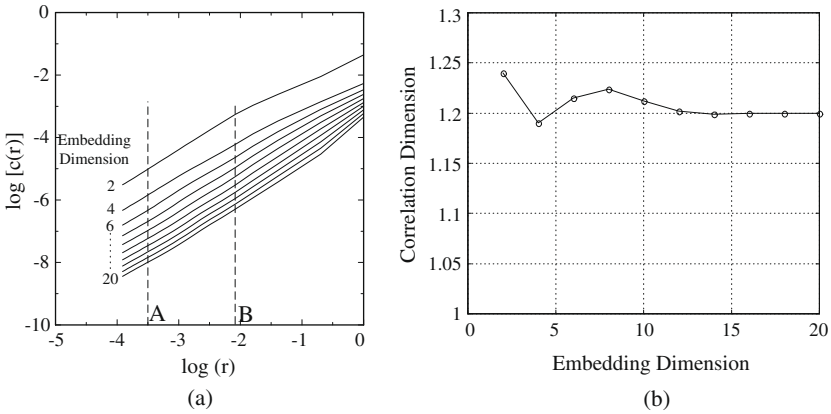

Fig. 8. Variation $c(r)$ with embedding dimension at $\boldsymbol{s}$ = 3.0 (a) and variation of correlation dimension with embedding dimension (b).

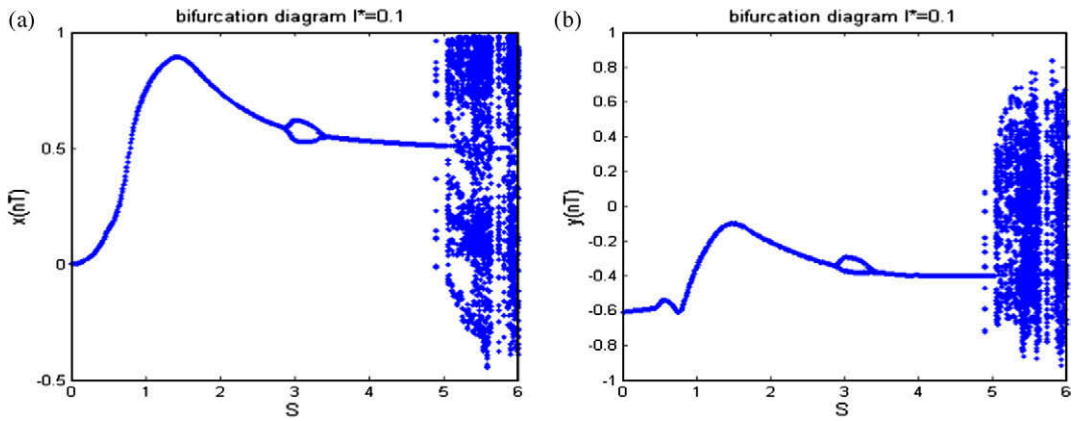

Fig. 9. Bifurcation diagram of $X(nT)$ (a) and $Y(nT)$ (b) versus rotor speed $\boldsymbol{s}$ (l^* = 0.1).

The supporting region of HSFD should be divided into three regions: static pressure region, rotating direction dynamic pressure region and axial direction dynamic pressure region, as shown in Fig. 2. In the part of HSFD with $-a \leqslant z \leqslant a$, the long bearing theory is assumed and Reynolds equation is solved with the boundary condition of static pressure region $p_{c,i}$ acquiring the pressure distribution $p_0(\theta)$. In the part of HSFD with $a \leqslant |\, z \,| \frac{L}{2}$, the short-bearing theory is assumed and solves the Reynolds equation with the boundary condition of $p(z,\theta)\,|_{z=\pm a} = p_0(\theta)$ and $p(z,\theta)|_{z=\pm L/2} = 0$, yielding the pressure distribution in axis direction dynamic pressure region $p(z,\theta)$. Finally, a formula of pressure distribution in whole supporting region is obtained.

According to the above conditions, the instant oil film pressure distribution is as follows.

The instant pressure in rotational direction within the range of $-a \leqslant z \leqslant a$ is

$$p_0(\theta) = \begin{cases} p_{c,i}; \frac{\pi}{2}(i-1) - \frac{\beta}{2} - \varphi_b \leqslant \theta \leqslant \frac{\pi}{2}(i-1) + \frac{\beta}{2} - \varphi_b \\ p_i(\theta); \frac{\pi}{2}(i-1) + \frac{\beta}{2} - \varphi_b \leqslant \theta \leqslant \frac{\pi}{2} i - \frac{\beta}{2} - \varphi_b \end{cases}, i = 1,2,3,4. \tag{8}$$

where

$$p_i(\theta) = p_{c,i} + \frac{6\mu R^2}{g(h,l)\delta^2}\frac{\dot{\varepsilon}}{\varepsilon}\left[\frac{1}{(1+\varepsilon\cos\theta)^2} - \frac{1}{(1+\varepsilon\cos\theta_{i1})^2}\right] + c_1\int_{\theta_{i1}}^{\theta}\frac{1}{g(h,l)\delta^3(1+\varepsilon\cos\theta)^3}d\theta - \int_{\theta_{i1}}^{\theta}\frac{12\dot{\varphi}_b\mu\delta\varepsilon R^2\cos\theta}{g(h,l)\delta^3(1+\varepsilon\cos\theta)^3}d\theta, i = 1,2,3,4 \tag{9}$$

$$c_1 = \frac{p_{c,i+1} - p_{c,i} - \frac{6\mu R^2}{g(h,l)\delta^2}\frac{\dot{\varepsilon}}{\varepsilon}\left[\frac{1}{(1+\varepsilon\cos\theta_{i2})^2} - \frac{1}{(1+\varepsilon\cos\theta_{i1})^2}\right] + \int_{\theta_{i1}}^{\theta_{i2}}\frac{12\dot{\varphi}_b\mu\delta\varepsilon R^2\cos\theta}{g(h,l)\delta(1+\varepsilon\cos\theta)^3}d\theta}{\int_{\theta_{i1}}^{\theta_{i2}}\frac{1}{g(h,l)\delta^3(1+\varepsilon\cos\theta)^3}d\theta},$$

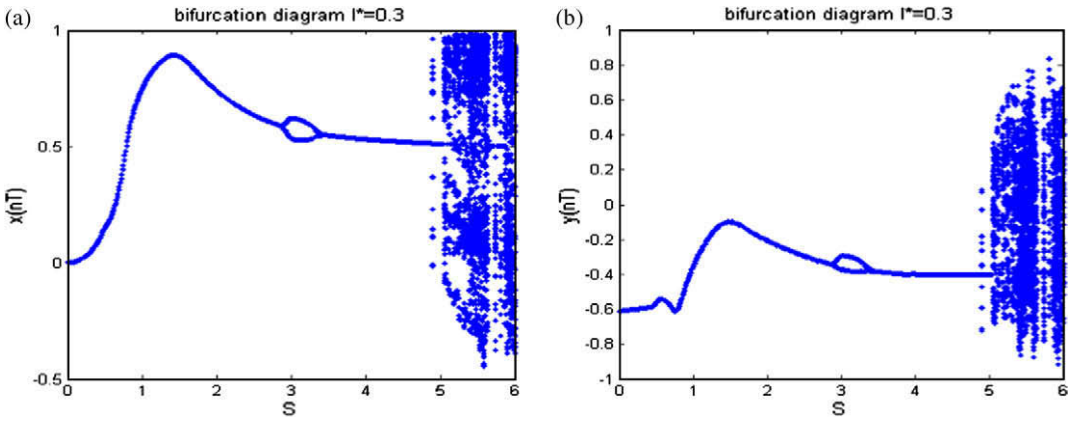

Fig. 10. Bifurcation diagram of $X(nT)$ (a) and $Y(nT)$ (b) versus rotor speed s ($l^* = 0.3$).

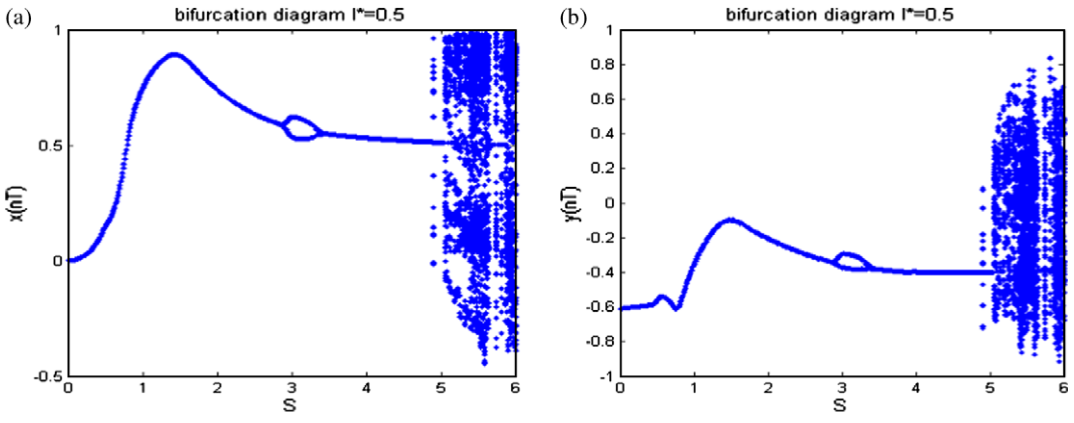

Fig. 11. Bifurcation diagram of $X(nT)$ (a) and $Y(nT)$ (b) versus rotor speed s ($l^* = 0.5$).

$$\theta_{i1} = (i-1)\frac{\pi}{2} + \frac{\beta}{2} - \varphi_b, \theta_{i2} = i\frac{\pi}{2} - \frac{\beta}{2} - \varphi_b, \quad i = 1,2,3,4.$$

The instant pressure in the axis direction within the range of $a \leqslant |z| \leqslant \frac{L}{2}$ is

$$p(\theta,z) = \left(\frac{L}{2} - |z|\right)\left\{[A_1(\theta)\dot{\varphi}_b\varepsilon + A_2(\theta)\dot{\varepsilon}](a-|z|) + p_0(\theta)\frac{1}{L/2-a}\right\}. \tag{10}$$

where

$$A_1(\theta) = \frac{6\mu\delta\sin\theta}{g(h,l)\delta^3(1+\varepsilon\cos\theta)^3}; \quad A_2(\theta) = \frac{6\mu\delta\cos\theta}{g(h,l)\delta^3(1+\varepsilon\cos\theta)^3}.$$

2.3. Solution of the instant oil film supporting force

The instant oil film forces of the different elements are determined by integrating Eqs. (8) and (10) over the area of the journal sleeve. In the static pressure region, the forces are

$$F_{rs} = \sum_{i=1}^{4} p_{ci} 2aR\left[\sin\left(\frac{\pi}{2}(i-1) + \frac{\beta}{2} - \varphi_b\right) - \sin\left(\frac{\pi}{2}(i-1) - \frac{\beta}{2} - \varphi_b\right)\right], \tag{11}$$

$$F_{\tau s} = \sum_{i=1}^{4} p_{ci} 2aR\left[\cos\left(\frac{\pi}{2}(i-1) - \frac{\beta}{2} - \varphi_b\right) - \cos\left(\frac{\pi}{2}(i-1) + \frac{\beta}{2} - \varphi_b\right)\right]. \tag{12}$$

In the rotational direction dynamics pressure region, the forces are

$$F_{rc} = \sum_{i=1}^{4} \int_{\theta_{i1}}^{\theta_{i2}} p_i(\theta) R2a\cos\theta d\theta, \tag{13}$$

$$F_{\tau c} = \sum_{i=1}^{4} \int_{\theta_{i1}}^{\theta_{i2}} p_i(\theta) R2a\sin\theta d\theta. \tag{14}$$

In the axial direction dynamic pressure region, the forces are

$$F_{ra} = \int_{-L/2}^{-a} dz \int_0^{2\pi} p(\theta,z) R\cos\theta d\theta + \int_{L/2}^{a} dz \int_0^{2\pi} p(\theta,z) R\cos\theta d\theta, \tag{15}$$

$$F_{\tau a} = \int_{-L/2}^{-a} dz \int_0^{2\pi} p(\theta,z) R\sin\theta d\theta + \int_{L/2}^{a} dz \int_0^{2\pi} p(\theta,z) R\sin\theta d\theta. \tag{16}$$

The resulting damper forces in the radial and tangential directions are determined by summing the above supporting forces. It is as follows

$$F_r = F_{rs} + F_{rc} + F_{ra}, \tag{17}$$

$$F_\tau = F_{\tau s} + F_{\tau c} + F_{\tau a}. \tag{18}$$

2.4. PD controller design

In order to control the hybrid squeeze-film damper bearing, two pairs of PD controllers are applied in the hydrostatic chambers to stabilize the hybrid squeeze-film damper bearing-rotor system. Assume that the pressure difference of hydrostatic chambers 1 and 3 is $\Delta p_1 = k_p x + k_d \dot{x}$ and the pressure difference of hydrostatic chambers 2 and 4 is $\Delta p_2 = k_p y + k_d \dot{y}$. The controllable pressure distributions in the hydrostatic chambers are

$$p_{c,1} = p_s - \Delta p_1, \quad p_{c,2} = p_s - \Delta p_2, \quad p_{c,3} = p_s + \Delta p_1 \quad \text{and} \quad p_{c,4} = p_s + \Delta p_2. \tag{19}$$

Substituting the pressure distributions in the hydrostatic chambers (19) into Eqs. (8)–(18), the resulting damper forces in the radial and tangential directions can be obtained.

3. Numerical studies

The numerical analysis is carried out by using the 4th order Runge-Kutta method. In this study, the time step for direct numerical integration is specified as $\pi/300$. Note that the time series data of the first 800 revolutions of the rotor are deliberately excluded from the dynamic behavior investigation to ensure that the data used corresponds to the steady state. These data are then used to generate the Poincaré map and bifurcation diagram.

In this study, 30,000 data points from the time series of the horizontal displacement of bearing center are used to construct the attractors in embedding space. The optimum delay time was found by autocorrelation function to be about one third of a revolution of the rotor. The fractal dimension of the system can be determined using the plot of ($\log \boldsymbol{c}(\boldsymbol{r})$) versus ($\log \boldsymbol{r}$), where $c(r)$ is the correlation function and $\boldsymbol{r}$ is the radius of an N-dimensional hyper-sphere. The number of points is chosen under a compromise between computation time and accuracy of the results. Following the method of Smith, the number of points used to estimate the dimension in this paper is less than 42^M, where M is the greatest integer less than the fractal dimension of the attracting set.

4. Results and discussion

4.1. Without couple stress fluid lubrication

In this section, the following values for the parameters are used:

$U = 0.5$, $B = 0.3$, $D = 0.005$, $k_p = 50{,}000$, $k_d = 100$, $p_s = 1{,}000{,}000$, $\varepsilon_0 = 0.68$ ($X_0 = 0.0$, $Y_0 = -0.68$) [22].

Fig. 3 is the bifurcation diagrams for an increased static misalignment of $\varepsilon_0 = 0.68$ ($X_0 = 0.0$, $Y_0 = -0.68$) at values of s within the range of 0.1–5.0. It can be seen that the T-periodic motion in both X and Y directions drop to a lower spatial displacement mode at the speed $s = 2.18$. The T-periodic motion loses its stability at $s = 2.54$ and a 2T-periodic motion occurs. The 0.5-subharmonic motion at 2.7 is shown in Fig. 4.1. It can be seen that there are two discrete points in the Poincaré map and peaks at 0.5 in the power spectrum. At speed $s = 2.72$, the 2T-periodic motion disappears and the 4T-periodic motion is generated. The two double loops of rotor trajectory, Poincaré map and power spectrums in X and Y directions at s = 2.8 are shown in Fig. 4.2(a)–(d). It can be seen that there are four return points in the Poincaré map and peaks at 0.25 in the

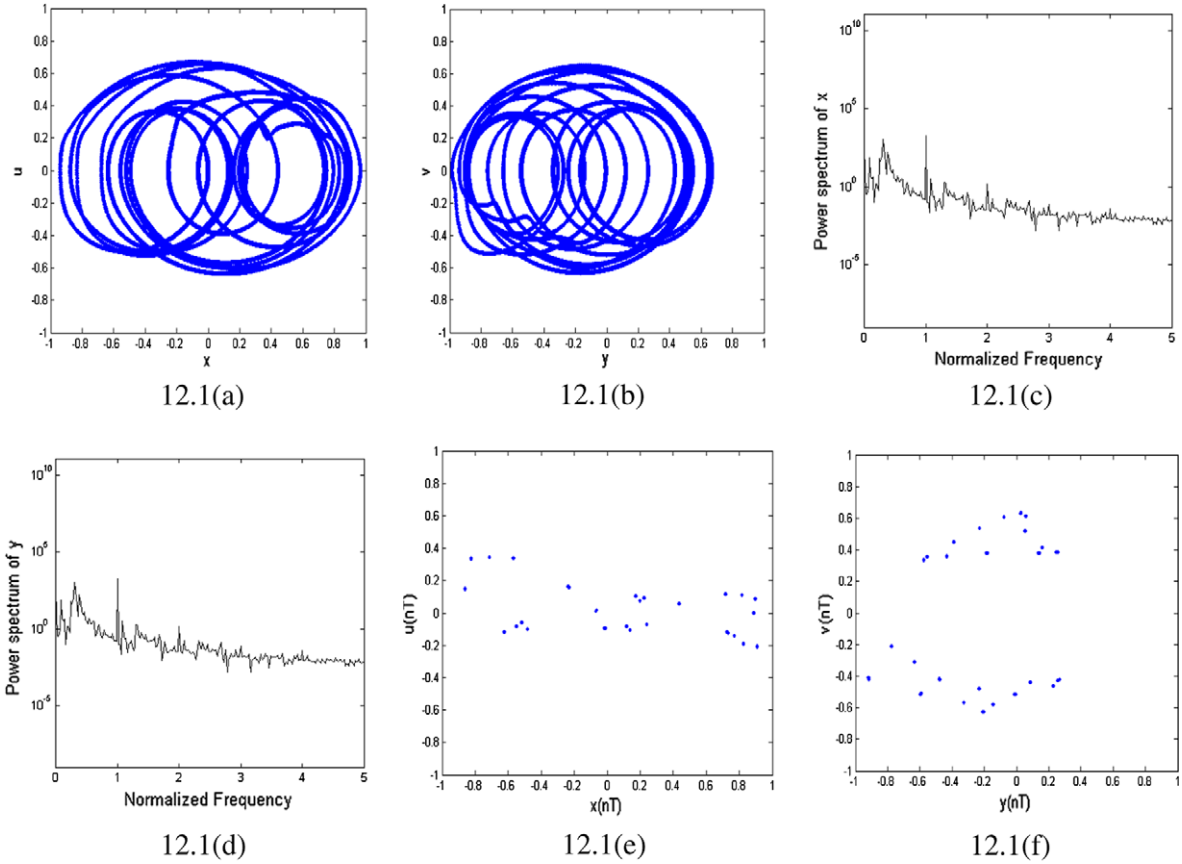

Fig. 12.1. Trajectory and Poincaré maps of bearing center and rotor center at $s = 4.9$ ($l^* = 0.3$).

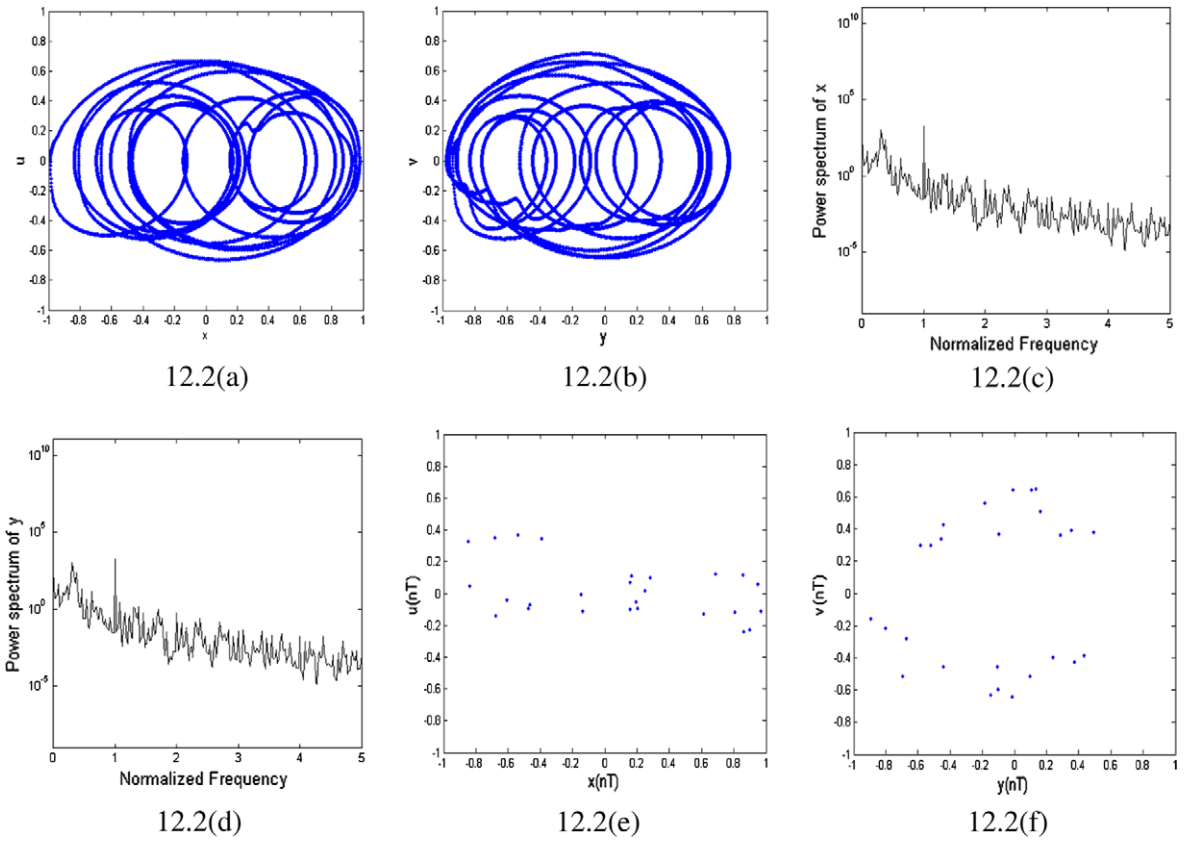

Fig. 12.2. Trajectory and Poincaré maps of bearing center and rotor center at $s = 5.1$ ($\bar{l}^* = 0.3$).

power spectrum. At $s = 2.81$, the 4T-periodic motion loses its stability and an 8T-periodic motion is built. The dynamics of rotor trajectory at $s = 2.82$ is shown in Fig. 4.3(a)–(d). It can be seen that there are eight return points in the Poincaré map and peaks at 0.125 in the power spectrum. When s is increased to 2.835, aperiodic motion disappears. At $s = 3.0$, the rotor trajectory, power spectrum, time series and Poincaré maps are shown in Fig. 5. It can be seen that the rotor trajectory is disordered and the power spectra in the X and Y directions are rich and broad. The time series in X and Y directions are irregular and the Poincaré maps for 1000 revolutions indicate possible strange attractors. The pressure distributions in the four oil chambers are shown in Fig. 6. It can be seen that the variations of pressure distributions are aperiodic. Fig. 7 reports the diagram of the maximum Lyapunov exponent. It can be seen that the steady-state value of the maximum Lyapunov exponent is 0.07, which confirms the chaotic nature of the motion at this operation condition. Fig. 8(a) shows the plot of ($\log c(r)$) versus ($\log r$) for different embedding dimensions at $s = 3.0$. It is clear that as the embedding dimension is increased, the linear part of the slope approaches a constant value. This is indicated in Fig. 8(b) where the steady-state value of these curves is the optimum estimated dimension of the rotor trajectory in the Y direction. It is found that the approximate dimension is about 1.2 at $s = 3.0$. A fractal dimension of this order for the rotor trajectory indicates that the dynamics exists on a finite low dimensional attractor. A positive maximum Lyapunov exponent and a fractal value of dimension both are the typical result for chaotic flow in this system. As the speed is further increased, the aperiodic motion disappears and a T-periodic motion suddenly appears at $s = 3.56$. The rotor trajectory, Poincaré map and power spectrums at $s = 4.0$ are shown in Fig. 4.4(a)–(d). It can be seen that only one point exists in the Poincaré map.

4.2. With couple stress fluid lubrication

Figs. 9–11 are bifurcation diagrams for different dimensionless parameters $\bar{l}^*$ in the horizontal and vertical directions. Comparing with the simulation results of $\bar{l}^* = 0.0$ (i.e. Newtonian fluid) show that the dynamic responses of couple stress lubricating system will more stable than usage of Newtonian fluid. It presents that the dynamic motions will be periodic or subharmonic motions before operating in very high rotating speed. It demonstrated that the usage of couple stress fluid may improve or escape undesired vibration conditions. The simulation results can evidence that dynamic response is chaotic motion at high speed ratio ($s = 4.9$, 5.1 and 6.0) from the bifurcation diagrams, dynamic trajectories, power spectrum, Poincaré

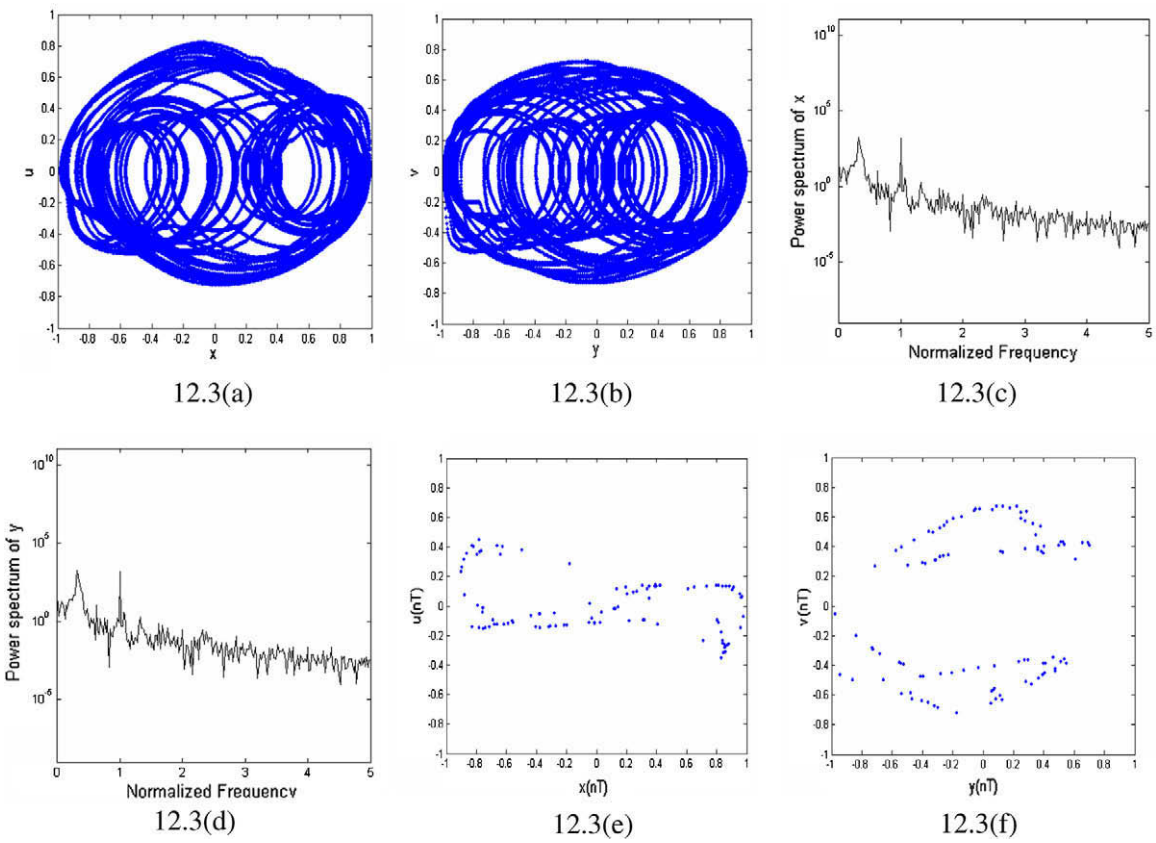

Fig. 12.3. Trajectory and Poincaré maps of bearing center and rotor center at $s = 6.0$ ($l^* = 0.3$).

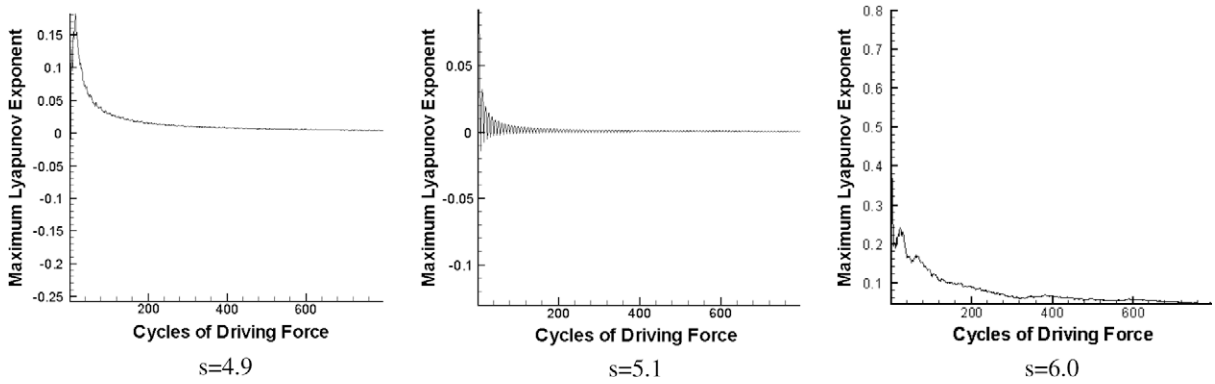

Fig. 13. The Maximum Lyapunov exponent plotted as a function of the number of drive cycles at different speed ratios. ($l^* = 0.3$).

section, and maximum Lyapunov exponent. From the evaluation of the five different methods, the outcome is consistent (see Figs. 12.1–12.3, 13).

4.3. With active control

In order to avoid the system to operate in a chaotic motion at $s = 3.0$, a suitable proportional gain k_p should be used. From Eq. (18), it can be seen that increasing the proportional gain k_p will get a larger pressure difference of hydrostatic chambers in both vertical and horizontal directions. By integrating larger pressure differences, larger resulting damper forces in the radial

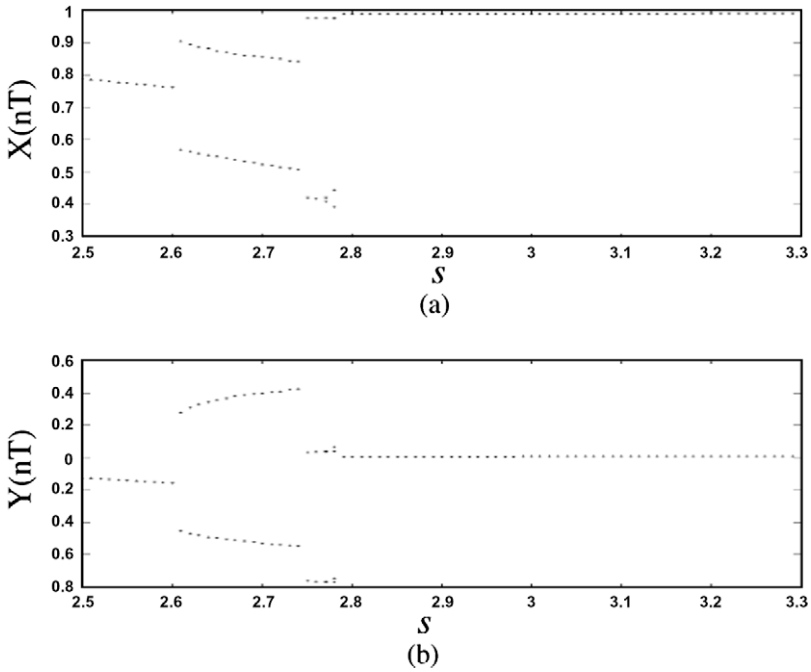

Fig. 14. Bifurcation diagram of $X(nT)$ (a) and $Y(nT)$ (b) versus rotor speed $\boldsymbol{s}$ with $k_p = 75{,}000$.

and tangential directions can be obtained. Increasing the resulting damper forces will increase the ability to restrain the disorder behavior of journal center. By suitable adjusting, an increased proportional gain $k_p = 75{,}000$ is applied to control this system in this study. The bifurcation diagrams in X and Y directions with $k_p = 75{,}000$ are shown in Fig. 14(a) and (b). It can be

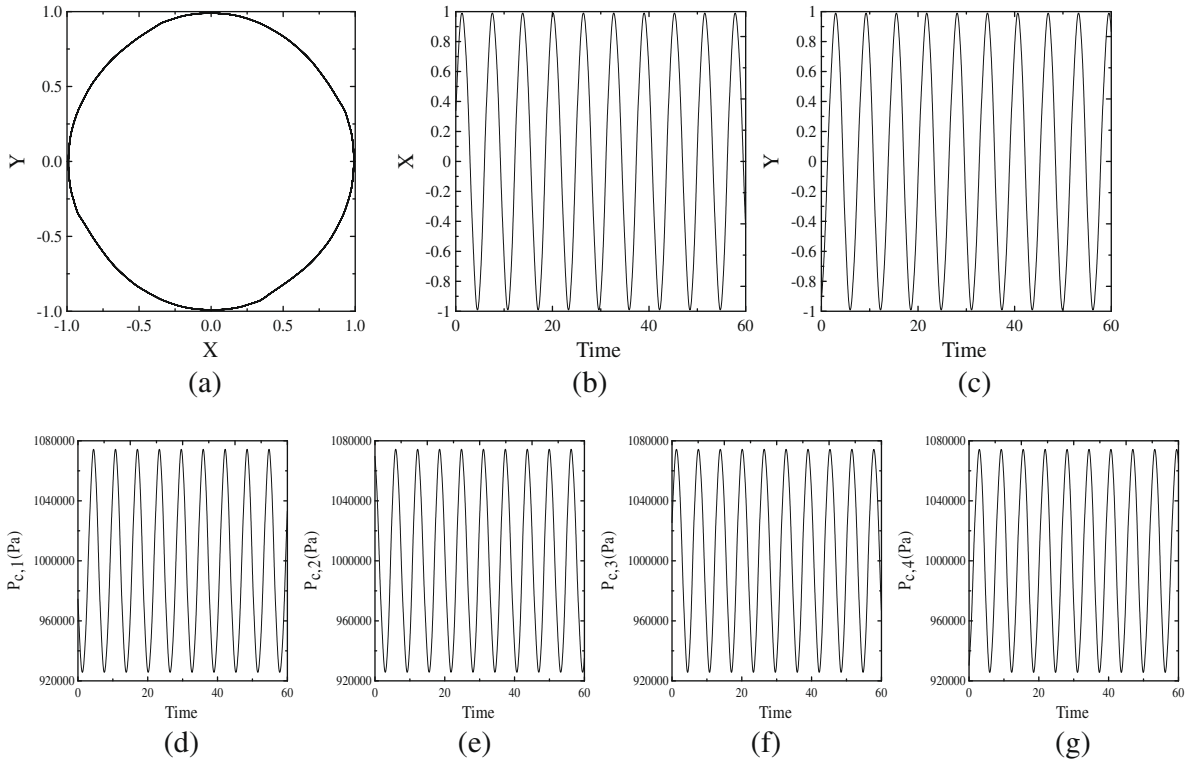

Fig. 15. Synchronous motion of rotor trajectory at $\boldsymbol{s} = 3.0$ with $k_p = 75{,}000$; (a) rotor trajectory; (b) and (c) time series of rotor trajectory; (d)–(g) pressure distributions in the static pressure chambers.

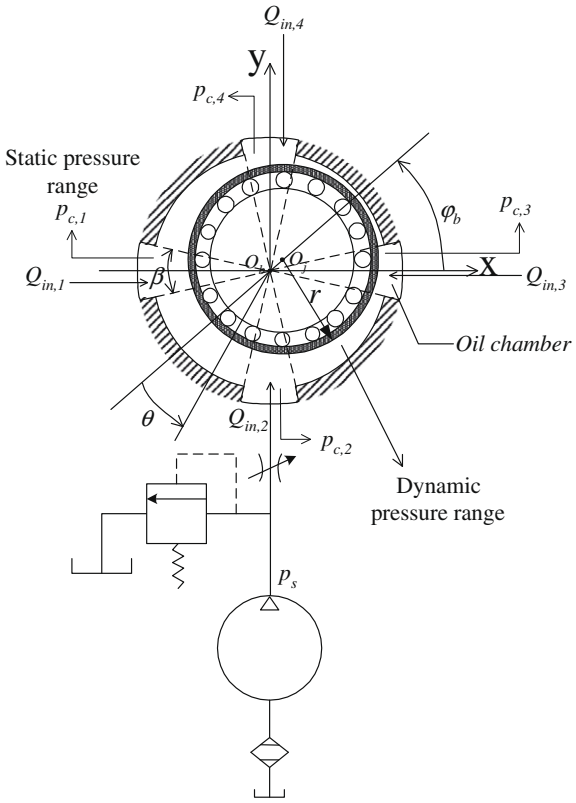

Fig. 16. The structure of electhydraulic controllable orifice with actuator (only shows the part in oil chamber 2).

seen that the rotor trajectory is T-periodic motion at s=3.0. It shows that the aperiodic motion disappears at this operating condition with k_p = 75,000. The rotor trajectory, time series in X and Y directions, and pressure distributions in the static pressure chambers are shown in Fig. 15.

5. Conclusions

The bifurcation and chaos of the unbalanced response of a rigid rotor supported by squeeze-film damper and lubricated with couple stress fluid under active control have been studied in this paper. The system state trajectory, the Poincaré maps, the power spectra, and the bifurcation diagrams were used to analyze the dynamic behavior of this system. The analysis demonstrates a complex dynamic behavior, which is manifested by an existence of periodic, subharmonic and aperiodic response of the rotor trajectory. Couple stress fluid can improve dynamic responses of the whole system or help it escape undesired motions. At the speed of s = 3.0, the maximum Lyapunov exponent is positive and Poincaré maps demonstrated a fractal structure. It shows that the trajectory of the rotor is in a state of chaos at this speed. In order to avoid the system operating in a nonsynchronous motion, an increased proportional gain k_p = 75,000 is applied to control this system. It can be seen that the rotor trajectory leave the disordered state and turns to a T-periodic motion at s=3.0 with k_p = 75,000. Compared with the results of Zhao et al. [3], it shows that the undesirable quasi-periodic motion disappears in the proposed HSFD system with increasing proportional gain k_p. It also shows that the range of 2T-periodic motions in the HSFD system is comparatively small.

It is known that if a rotor-bearing system operates in the state of aperiodic motion, the resulting broadband vibration with irregularly large vibrational amplitude will enhance the probability of fatigue failure. In this study, the results showed that the affects of undesirable non-synchronous vibrations in SFD system could reduced by the designed of HSFD system with active control. The suitable two pairs of PD controllers in static chambers can be realized by the two pairs of electrohydraulic controllable orifice with actuator as shown in Fig. 16. The effect of the actuator performance could be neglected if the response behavior of electrohydraulic orifice is fast enough.

Acknowledgment

The authors would like to thank for the help of Prof. Cha'o-Kuang Chen and reviewers' great recommendations.

References

[1] C.L. Chen, H.T. Yau, Chaos in the imbalance response of a flexible rotor supported be oil film bearings with non-linear suspension, Nonlinear Dynam. 16 (1998) 71–90.
[2] J.I. Nikolajsent, R. Holmes, Investigation of squeeze-film isolators for the vibration control of a flexible rotor, Trans. ASME J. Mech. Sci. 21 (4) (1979) 247–252.
[3] J.Y. Zhao, I.W. Linnett, L.J. Mclean, Subharmonic and quasi-periodic motion of an eccentric squeeze film damper-mounted rigid rotor, ASME J. Vib. Acoust. 116 (1994) 357–363.
[4] C.W. Chang-Jian, C.K. Chen, Chaos and bifurcation of a flexible rub-impact rotor supported by oil film bearings with non-linear suspension, Mech. Mach. Theory 42 (3) (2007) 312–333.
[5] C.W. Chang-Jian, C.K. Chen, Bifurcation and chaos of a flexible rotor supported by turbulent journal bearings with non-linear suspension, Trans. IMechE J-J. Engrg. Tribol. 220 (2006) 549–561.
[6] C.W. Chang-Jian, C.K. Chen, Nonlinear dynamic analysis of a flexible rotor supported by micropolar fluid film journal bearings, Int. J. Engrg. Sci. 44 (2006) 1050–1070.
[7] C.W. Chang-Jian, C.K. Chen, Bifurcation and chaos analysis of a flexible rotor supported by turbulent long journal bearings, Chaos Solitons Fractals 34 (2007) 1160–1179.
[8] C.W. Chang-Jian, C.K. Chen, Nonlinear numerical analysis of a flexible rotor equipped with squeeze couple stress fluid film journal bearings, Acta Mech. Solida Sin. 20 (4) (2007) 283–290.
[9] D.R. Oliver, Load enhancement effects due to polymer thickening in a short model journal bearings, J. Non-Newtonian Fluid Mech. 30 (1988) 185–196.
[10] H.A. Spikes, The behaviour of lubricants in contacts: current understanding and future possibilities, Proc. Instn. Mech. Engrs., J: J. Engrg. Tribol. 28 (1994) 3–15.
[11] V.K. Stokes, Couple-stresses in fluids, Phys. Fluids 9 (1996) 1709–1715.
[12] G. Ramanaiah, Slider bearings lubricated by fluids with couple stress, Wear 52 (1979) 27–36.
[13] R.S. Gupta, L.G. Sharma, Analysis of couple stress lubricant in hydrostatic thrust bearings, Wear 48 (1988) 257–269.
[14] E.F.E. Shehawey, K.S. Mekheimer, Couple-stresses in peristaltic transport of fluid, J. Phys.: D: Appl. Phys. 27 (1994) 1163–1170.
[15] N.C. Das, Elastohydrodynamic lubrication theory of line contacts: couple stress fluid model, STLE Tribol. Trans. 40 (2) (1997) 353–359.
[16] N.C. Das, A study of optimum load-bearing capacity for slider bearings lubricated with couple stress fluids in magnetic field, Tribol. Int. 31 (7) (1998) 393–400.
[17] J.R. Lin, Squeeze film characteristics of long partial journal bearings lubricated with couple stress fluids, Tribol. Int. 30 (1) (1997) 53–58.
[18] J.R. Lin, Static and dynamic behaviour of pure squeeze films in couple stress fluid-lubricated short journal bearings, Proc., Instn. Mech. Engrs., J: J. Engrg. Tribol. 62 (1) (1997) 175–184.
[19] J.R. Lin, Static and dynamic characteristics of externally pressurized circular step thrust bearings lubricated with couple stress fluids, Tribol. Int. 32 (1999) 207–216.
[20] J.R. Lin, Linear stability analysis of rotor-bearing system: couple stress fluid model, Comput. Struct. 79 (2001) 801–809.
[21] N.B. Naduvinamani, P.S. Hiremath, G. Gurubasavaraj, Squeeze film lubrication of a short porous journal bearing with couple stress fluids, Tribol. Int. 34 (2001) 739–747.
[22] C.L. Chen, H.T. Yau, Y.H. Li, Subharmonic and chaotic motions of a hybrid squeeze-film damper-mounted rigid rotor with active control, ASME J. Vibr. Acoust. 124 (2002) 198–208.